

A Dataset for Evaluating Multi-spectral Motion Estimation Methods

Weichen Dai¹, Yu Zhang¹, Shenzhou Chen¹, Donglei Sun², and Da Kong¹

Abstract—Visible images have been widely used for indoor motion estimation. Thermal images, in contrast, are more challenging to be used in motion estimation since they typically have lower resolution, less texture, and more noise. In this paper, a novel dataset for evaluating the performance of multi-spectral motion estimation systems is presented. The dataset includes both multi-spectral and dense depth images with accurate ground-truth camera poses provided by a motion capture system. All the sequences are recorded from a handheld multi-spectral device, which consists of a standard visible-light camera, a long-wave infrared camera, and a depth camera. The multi-spectral images, including both color and thermal images in full sensor resolution (640×480), are obtained from the hardware-synchronized standard and long-wave infrared camera at 32Hz. The depth images are captured by a Microsoft Kinect2 and can have benefits for learning cross-modalities stereo matching. In addition to the sequences with bright illumination, the dataset also contains scenes with dim or varying illumination. The full dataset, including both raw data and calibration data with detailed specifications of data format, is publicly available.

I. INTRODUCTION

In recent years, vision-based motion estimation methods such as visual odometry (VO) [1] and visual simultaneous localization and mapping (vSLAM) [2] have attracted full attention for their diverse applications. These methods have been investigated in great detail for standard cameras, which can take advantage of rich textures only in bright illumination. For example, in scenarios such as data center inspection, firefighting, and rescue, standard cameras cannot provide sufficient information due to inadequate color textures, smog cover, or dim illumination. In complex illuminated environments, adding long-wave infrared (LWIR) cameras can complement the texture with information from another spectrum. Hence, the multi-spectral setup with these both cameras can become a reliable information source for all-day vision or fog-penetrating localization.

To evaluate the performance of various multi-spectral SLAM and odometry methods involving multi-spectral sources, a complete dataset with ground truth is necessary. Compared with the dataset for stereo standard cameras [3]–[5], the availability of a hardware-synchronized multi-spectral dataset is minimal. Moreover, stereo matching between RGB images and LWIR images remains a challenging problem due to the insufficiency of textures in thermal images and the difference between the modalities. Therefore,

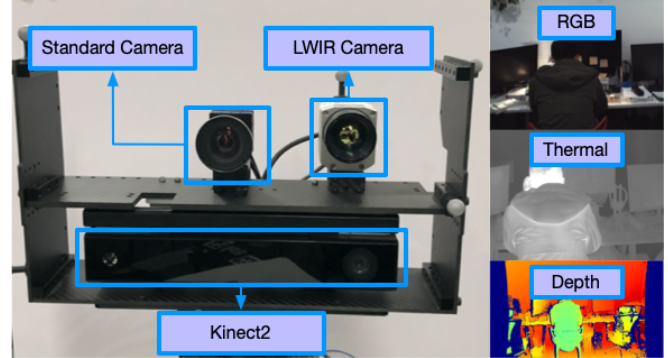


Fig. 1: The multi-spectral setup with Kinect2. *Left*: devices include an RGB camera, an LWIR camera, a Kinect2, and the markers of motion capture systems. *Right*: example color image, thermal image, and depth image from Kinect2.

the dataset should also provide reference stereo correspondences between different modalities.

In this paper, a multi-spectral dataset is provided for evaluating multi-spectral motion estimation methods. The dataset includes a set of sequences in diverse illumination conditions obtained on a setup consisting of a standard camera, an LWIR camera, and a Kinect2. In the dataset, each sequence contains the color, thermal, and depth images, as well as the ground-truth trajectory. The color and thermal images (640×480) are captured at 32Hz on hardware-synchronized devices. The depth images are provided by the Kinect2 camera [6] at 30Hz, enabling the projection of one image onto another. The ground-truth poses are recorded from a motion capture system at 120Hz. All sensors are calibrated carefully for higher accuracy.

The whole dataset, including the raw and calibration data, calibration files, and tool codes, is available on

<https://github.com/NGCLAB/multi-spectral-dataset>.

The main contributions of this paper are as follows:

- A new multi-spectral dataset with hardware-synchronized color and thermal images is provided for the evaluation of multi-spectral motion estimation systems.
- The additional depth images can be used to study stereo matching between the visible and LWIR spectra.

The rest of the paper is organized as follows. Related work is reviewed in Section II, and the platform is introduced in Section III. The calibration procedures to retrieve intrinsic and extrinsic parameters of each device are discussed in Section IV, and the details of time synchronization are

¹State Key Laboratory of Industrial Control Technology, College of Control Science and Engineering, Zhejiang University, {weichendai, zhangyu80, chenshenzhou, kongda1997}@zju.edu.cn

²Department of Aerospace Engineering, University of Illinois at Urbana-Champaign, dsun13@illinois.edu

presented in Section V. The dataset is described in VI, and the evaluation metrics are provided in Section VII. Finally, conclusions are drawn in Section VIII.

II. RELATED WORK

Several types of sensors have been used in motion estimation, including monocular standard cameras [7], [8], stereo standard cameras [9], event-cameras [10], and RGB-D cameras [11]. These motion estimation methods can be categorized into filter-based [12] and factor-graph-optimization-based methods [13]. The majority of these methods focus on utilizing the information on the visible spectrum.

Since the performance of standard cameras can be significantly influenced by illumination, LWIR cameras have been explored. With a different sensor modality, LWIR cameras are illumination independent, but they have their shortcomings. As mentioned in [14], the notable shortcomings include high noise, the unique mechanism that causes Non-Uniformity Correction (NUC) corruption, and high dynamic range. Due to these factors, the visual odometry using LWIR setups [15]–[17] usually cannot provide accurate results as those based on visible light in most environments. Hence, multi-spectral methods using LWIR cameras as complementary sensors have attracted extensive attention [18], [19] for their potential to function in poorly illuminated environments.

A publicly available dataset with ground truth is critical for evaluating the performance of multi-spectral motion estimation methods. For visible light sensors, there are several well-known datasets, where the illumination condition is usually stable. Depending on the application, the carriers may be handheld [20], cars [4], micro aerial vehicles [21], underwater vehicles [22], and moving robots [23]. For the task of fusing multi-sensor information, most datasets provide synchronized sensor data in addition to visible images [24]. Meanwhile, since hardware synchronization of sensors can increase performance [25], some datasets are obtained on hardware-synchronized devices. Among these datasets, the TUM monocular dataset is the first to take into account photometric calibration [5], [26]. Moreover, motion capture systems such as VICON¹ and OptiTrack² are used to obtain the ground truth in most datasets. In other datasets, the ground-truth trajectories are acquired through GPS or accurate 3D reconstruction.

Most of the existing multi-spectral datasets were generated for fundamental tasks such as detection [27], segmentation [28], tracking [29], stereo matching [30], and place recognition [31]. The KAIST multi-spectral dataset [32] was proposed for all-day vision tasks in outdoor environments covering a wide range from urban to residential regions. In most indoor environments, since thermal images cannot provide rich textures, it is more challenging to design multi-spectral motion estimation. Moreover, an indoor multi-spectral dataset with highly accurate ground truth for evaluation is still necessary. Meanwhile, since stereo matching

¹<http://www.vicon.com/>

²<http://optitrack.com/>

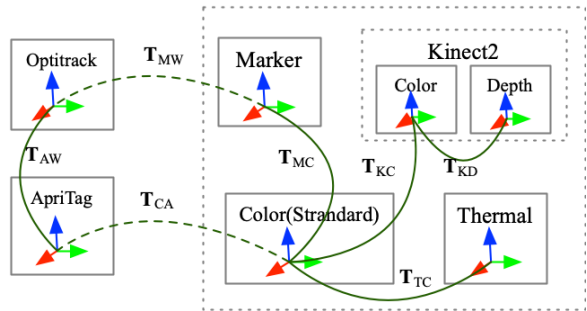


Fig. 2: Coordinate systems. The dotted rectangle contains all sensors which are rigidly connected with the color standard camera coordinate system. The solid lines denote rigid connections. The dashed lines indicate that relative transformations can be changed when the setup moves.

is the foundation of stereo methods, providing depth data plays an essential role in augmenting the development and validation of cross-modalities matching algorithms.

III. PLATFORM

The multi-spectral setup consists of a standard camera, an LWIR camera, and a Kinect2, as shown in Fig. 1. The coordinate frames are shown in Fig. 2. In the coordinate system, the following notations are used to represent each corresponding sensor:

- C: color standard camera
- T: LWIR camera
- K: color camera on Kinect2
- D: depth camera on Kinect2
- A: AprilTags board
- M: rigid body constructed from markers by OptiTrack
- W: world coordinate in OptiTrack

The transformation T_{JI} , $I, J \in \{A, C, D, K, M, T, W\}$, denotes the transformation from the coordinate frame on a device I to a device J .

The standard camera, thermal camera, and Kinect2 are rigidly connected to the rack with OptiTrack markers. Instead of a printed chessboard, a unique chessboard whose surface is made of different materials is used to calibrate the system. Meanwhile, the parameters between the motion capture system and the cameras are calibrated using a grid of AprilTags [33], which is static in the scene. In the following part, each hardware component is briefly described, and the necessary sensor information is summarized in Table I.

A. Multi-spectral device

The multi-spectral device consists of a standard camera and an LWIR camera. The former is an ImageSource DFK 22BUC03. It uses a global shutter and captures 640×480 RGB images at 32 Hz. Moreover, this camera can be synchronized by an external trigger signal. The LWIR camera is an Optris PI 640, which produces 16-bit 640×480 thermal images and outputs a frame-sync trigger signal at 32Hz. This frame-sync trigger signal is set as the external trigger signal via a hardware connection to the standard camera.

TABLE I: Sensors in the setup

Sensor	Model	Rate	Characteristics
Color standard camera	ImageSource	32Hz	global shutter 640×480 RGB32
LWIR camera	Optris	32Hz	130 mK 640×480 16-bit thermal Spectral range 7.5-13 μm Non-uniformity correction
Depth camera	Kinect2	30Hz	Time of Flight 960×540 16-bit depth
Motion caption system	OptiTrack	120Hz	6-D pose Four cameras

Therefore, this platform can provide synchronized color and thermal images at 32Hz when both cameras are set on trigger mode. The exposure time is set to the value less than the sensor synchronization period, which ensures that the captured images are at the same frequency.

B. Kinect2

For providing a reference for stereo matching between the visible and LWIR spectra, a Kinect2 is added to the setup. It integrates both color and depth cameras. The depth images are 960×540 and captured at 30Hz. Since Kinect2 follows the time of flight (ToF) measurement principle, the phase difference between the infrared illuminator and the infrared camera is used to compute the depth. The timestamp of the depth images is well aligned with the multi-spectral device by the software.

C. Motion capture system

To record accurate ground truth for the dataset, the OptiTrack motion capture system is used to provide 6D poses of the multi-spectral device. Four infrared motion capture cameras are installed to cover the whole 2m×2m workspace, and five markers are attached to the setup to create a virtual rigid body in OptiTrack. The motion capture system tracks the reflective markers by triangulation. Also, each motion capture camera has infrared LEDs to improve tracking performance. Therefore, for ensuring the accuracy of the depth images, these LEDs are kept out of Kinect2's sight in the acquisition process. Besides, it should also be ensured that the lens and the infrared emitter on the Kinect2 will not be detected as markers by mistake. These steps help to guarantee that the depth camera on Kinect2 and these motion capture cameras do not influence each other. Since the setup only moves within a small area, all sequences provide the ground truth.

IV. CALIBRATION

All sensors in the setup require calibration for the localization. The calibration involves the intrinsic parameters of each camera and the extrinsic parameters between cameras, as shown in Fig. 2 in solid lines. In this section, how to calibrate these cameras is introduced.

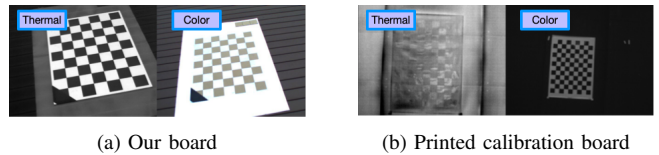


Fig. 3: Multi-spectral calibration board. A unique chessboard with the surface made of different materials can provide distinctive textures in both spectra.

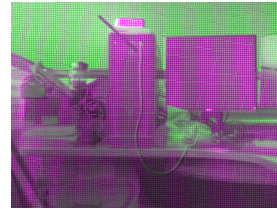


Fig. 4: Multi-spectral registration checking. The blue channel of the color image is replaced with the thermal value using obtained intrinsics and extrinsics with an assumed depth of 2m.

A. Calibration of the multi-spectral device

Due to the difference in information sources, the conventional printed board used to calibrate standard cameras cannot yield high contrast between textures in the thermal image. Therefore, specialized equipment needs to be designed for calibration. There are two calibration methods: active [34], [35] and passive [16]. Active methods heat part of the calibration equipment to generate different thermal radiations. Passive methods do not depend on active heating.

Since active methods are inconvenient and complicated, a passive method is used for this setup. Exploiting the difference in the reflection on metal and non-metal materials on both LWIR and visible spectra, an aluminum board with fiber squares on it is designed for calibration. This board provides distinct edges and excellent contrast, as shown in Fig. 3. During the calibration, the device followed a stop-capture-go manner to eliminate the error introduced by unsynchronized data. The intrinsic and extrinsic parameters of the multi-spectral device are obtained using Matlab[®] tools [36]. Based on the calibration results, the registration checking can be tested, as shown in Fig. 4.

B. Calibration of the Kinect2

The calibration of the Kinect2 follows two steps. The intrinsic and extrinsic parameters between the two cameras inside the Kinect2 is calibrated first. The extrinsic parameters between the Kinect2 and the standard camera are then calibrated.

The Kinect2 has two cameras: a color camera and a depth camera, the latter of which is a near-infrared (NIR) camera. Since the NIR spectrum is next to the visible spectrum, both spectra share similar textures. Therefore, the printed chessboard can be directly used to calibrate these two cameras, as shown in Fig. 5. The difficulty in image capture lies in that the NIR light emitter cannot be turned off,

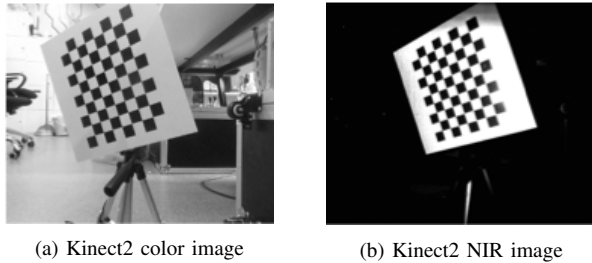


Fig. 5: Chessboard for Kinect2 calibration. The board provides distinctive squares for both cameras. Because of the active light, a huge contrast between the board and the background is presented in the NIR image.

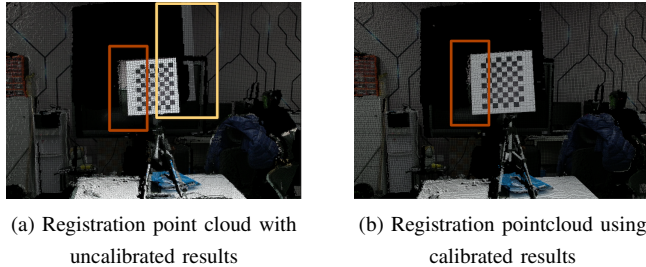


Fig. 6: Registration results of Kinect2. The yellow box shows the area with wrong depth values. The area in the red box is the edge of the object, which has more significant uncertainty for Kinect2 since the depth changes a lot. Under uncalibrated parameters, the yellow and red boxes show a wrong texture mapping. After calibration, the color and depth data of the object edges are well matched.

and hence additional effort is required. Meanwhile, to obtain clear NIR texture, the illumination should also be adjusted appropriately.

With obtained color and NIR image pairs, the intrinsic and extrinsic parameters of the Kinect2 can be computed. Since the depth camera can provide 3-D information, the point cloud can be registered with the corresponding color image. As shown in Fig. 6, the color and depth images are well-matched after calibration, except for the noise on the edges of objects. Similarly, the calibration between the standard camera and the Kinect2 can also be obtained. The only difficulty is that the field of view (FoV) of the Kinect2 color camera is much larger than that of the standard camera. Hence, it is necessary to cover the Kinect2's FOV as much as possible during data acquisition.

C. Calibration of the motion capture system

For calibrating the motion capture system, a calibration wand with three markers (shown in Fig. 7) needs to be waved around the working area. Through the tracking results of these three markers, the software provided by OptiTrack computes the intrinsic and extrinsic parameters of all motion capture cameras. For calibrating the extrinsic parameters between the multi-spectral cameras and the motion capture frame, which is equivalent to estimating the relative pose \mathbf{T}_{WC} , \mathbf{T}_{MC} should be found first. \mathbf{T}_{MC} is computed

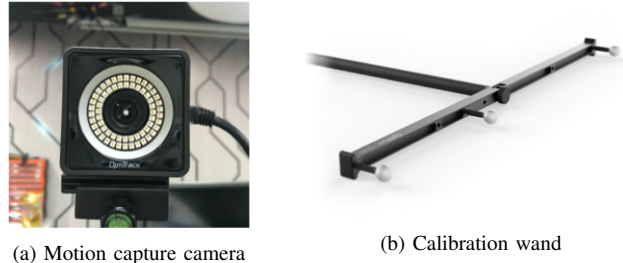


Fig. 7: Motion capture system from OptiTrack. There are four motion capture cameras to track the 3D position of passive reflective markers. The system requires calibration using the wand.

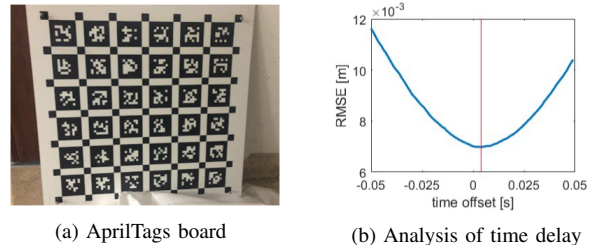


Fig. 8: (a) AprilTags board used for calibration and time synchronization. Four reflective markers are attached to the four small corner squares of the board. (b) The time delay between the motion capture system and the standard camera.

through the hand-eye calibration using a non-linear least square procedure. This procedure requires the knowledge of \mathbf{T}_{WA} and \mathbf{T}_{AC} . \mathbf{T}_{WA} is obtained through the four markers on the AprilTags board shown in Fig. 8(a), and \mathbf{T}_{AC} is computed from the tags on the board. With these relative transformations, \mathbf{T}_{MC} can be calibrated, and \mathbf{T}_{WM} can be converted to the poses \mathbf{T}_{WC} .

V. TIME SYNCHRONIZATION

In the evaluation data, every sensor should be synchronized with the standard camera since incorrectly paired images will introduce error. Besides the camera calibration discussed in Sec. IV, the stop-capture-go manner was adopted to avoid time compensation, which also ensures the accuracy of the calibration.

High-accuracy hardware-synchronization is achieved on the multi-spectral device using the frame-sync signal, which is generated by the LWIR camera. Upon the rising pulse, the image from the standard camera is captured. An experiment is designed to check the performance of the synchronization. In this experiment, a ball is released in front of the board. As shown in Fig. 9, both cameras can capture the same scene with little time delay. The actual difference between the timestamps of those two images is less than 1ms. Therefore, the timestamps of both images need no modifications in the dataset.

It should be noted that those two cameras work with different exposure times. The exposure time of the LWIR camera is longer than that of the standard camera. Therefore

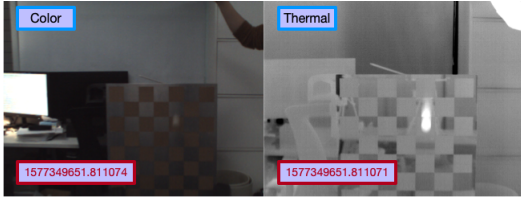


Fig. 9: Hardware-synchronized multi-spectral images. In both images, the ball in the red box indicates that two cameras can capture images almost simultaneously. Among most pairs, the thermal images are captured approximately 1ms later than the color images.

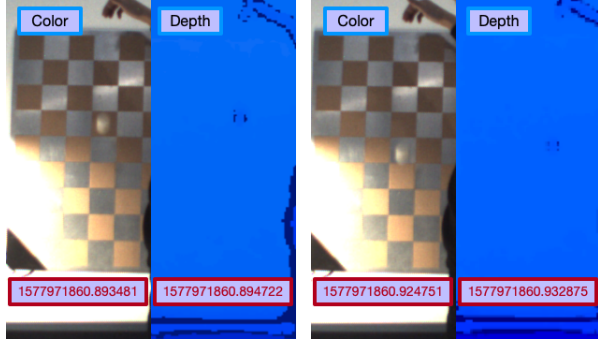


Fig. 10: Images from the standard camera and the depth camera. The timestamps in those red boxes indicate that the depth images are captured slightly later than the color images.

the exposure time of the standard camera is fixed to reduce the error caused by exposure time fluctuations.

For the Kinect2 and the standard camera, the depth images are captured on average a little later than the color images, as shown in Fig. 10. The delay in the depth images is negligible, and no correction is required before data association.

The time delay between the motion capture system and the standard camera needs also be determined before the localization results can be evaluated. The time delay can be determined from the residuals of different time delays. As shown in Fig. 8(b), the poses from the motion capture system are approximately 4ms earlier than the images from the standard camera. The time delay is also trivial, and hence it is not necessary to modify the timestamps of the raw poses.

VI. DATASET

The dataset includes both the evaluation sequences and the calibration data, as summarized in Table II. In the calibration data, both the raw data and our calibration results are provided.

The dataset includes the following categories:

- Calibration:
 - *visible-LWIR*: the calibration data to compute the intrinsics and extrinsics of the multi-spectral device. The board shown in Fig. 3 is recorded in a stop-capture-go manner with changing viewpoints and small camera motion.

TABLE II: List of multi-spectral sequences

Sequence Name	Duration [s]	Avg. Trans. Vel. [m/s]	Avg. Rot. Vel. [deg/s]
Bright illumination			
desk1-halfsphere	68.3495	0.1266	13.2977
desk1-rpy	61.400	0.0524	15.6739
desk1-static	25.2803	0.0014	1.2815
desk1-xyz	48.5500	0.1662	12.5325
desk2-circle	34.5399	0.1261	9.7276
desk2-halfsphere	44.3201	0.0965	8.6699
desk2-rpy	47.7005	0.0450	13.3737
desk2-static	33.3701	0.0113	2.6567
desk2-xyz	44.9602	0.1492	8.2026
desk1-circle-person	33.8101	0.2060	13.3581
desk1-halfsphere-person	76.9798	0.1097	10.7502
desk1-rpy-person	60.0997	0.0484	15.7353
desk1-rpy-person-slow	59.5304	0.0448	18.3272
desk1-static-person	19.9794	0.0020	1.4005
desk1-xyz-person	51.1640	0.1422	11.9822
desk1-halfsphere-dy	64.0704	0.1425	13.0772
desk1-rpy-dy	48.4592	0.0546	14.5771
desk1-static-dy	24.9294	0.0013	0.4209
desk1-xyz-dy	48.7687	0.1542	7.5778
Varying illumination			
desk1-rpy-ic	62.8403	0.0485	15.5414
desk1-halfsphere-ic	73.5899	0.1125	12.2998
desk1-static-ic	27.6798	0.0015	0.4493
desk1-static-ic-lampon	24.7401	0.0009	0.4519
desk1-xyz-ic	67.2905	0.1243	9.6570
desk2-circle-ic	30.1300	0.1246	7.5655
desk2-rpy-ic	64.8807	0.0475	10.9869
desk2-static-ic	23.9501	0.0348	5.4931
desk2-xyz-ic	52.1794	0.1150	11.8753
desk1-halfsphere-ic-person	66.9900	0.1158	13.6747
desk1-rpy-ic-person	56.2300	0.0464	16.4843
desk1-static-ic-person	33.8796	0.0082	2.6343
desk1-xyz-ic-person	54.1956	0.1550	11.9565
Dim illumination			
desk1-halfsphere-dim	69.2399	0.1348	12.6894
desk1-halfsphere-dim2	67.8903	0.1346	11.7965
desk1-rpy-dim	48.0199	0.0490	14.6452
desk1-rpy-dim2	52.5703	0.0501	13.9791
desk1-static-dim	21.5306	0.0009	0.2913
desk1-static-dim2	19.4200	0.0028	1.4049
desk1-xyz-dim	53.6903	0.1463	7.5768
desk1-xyz-dim2	53.8106	0.1564	7.5196

- *visible-Kinect*: the calibration data to find the intrinsics and extrinsics of Kinect2 and to obtain the transformations between Kinect2 and the standard camera.

- Evaluation:

- *bright room*: sequences captured inside a bright room where the color images contain rich textures.
- *room with dynamic illumination*: sequences captured inside a room with dynamic illumination, where the quality of the color images is not guaranteed.
- *dark room*: sequences captured inside a dark room. The color images do not provide clear visible textures.

A. Sequences

The dataset was acquired in indoor office environments, as shown in Fig. 11. The sequences can be classified according to three criteria: illumination, motion, and the presence of a person in the image.

1) *Illumination*: Novel methods can be evaluated in environments with different illumination conditions. Accordingly, in addition to the sequences recorded in bright environments, the sequences with the suffix *-ic* in the name contain data with lights turned on and off randomly. Moreover, for testing the performance of multi-spectral methods in extreme illu-

mination conditions, the sequences with suffix *-dim* contain data where the scene is dark.

2) *Motion*: These sequences are intended to evaluate methods with separated motions along and around the principal axes of the setup. There are five types of camera motion:

- * *-halfsphere* denotes that the camera moves along the trajectory of a halfsphere with a diameter of 1m.
- * *-xyz* denotes that the camera moves approximately along the x , y , and z axes.
- * *-rpy* denotes that the camera only rotates with roll, pitch, and yaw motion.
- * *-circle* denotes that the camera moves approximately around a circle.
- * *-static* denotes that the camera is nearly motionless.

3) *Person*: Since the temperature of the objects in the office is almost uniform, the LWIR camera cannot provide rich textures. Since the temperature of the human body differs significantly from the environment, a person in the FoV of the camera can provide striking contrasts in textures in the thermal images. Hence, in the sequence with the suffix *-person*, a person sitting in front of a desk. Otherwise, the environment only contains static objects at room temperature.

4) *Dynamic*: In the sequences with the suffix *-dy*, a person is walking around in front of the setup to add disturbances. These data can be used to test the robustness of the multi-spectral system in dynamic environments since moving objects in the environment may lead to the failure of motion estimation.

5) *Desk*: As shown in Fig. 12, two desks marked as *desk1* and *desk2* are used as targets with different backgrounds.

B. Data format

Each sequence is saved as an ROS bag file.

1) *ROS Bag Files*: These bag files contain raw data recorded in the following topics:

- */camera/image_raw*: color images from the standard camera
- */optris/thermal_image*: thermal images from the LWIR camera
- */camera/flag_state*: flag states of the LWIR camera
- */kinect2/image_depth_rect_raw*: color images from Kinect2
- */kinect2/image_depth_rect_raw*: depth images from Kinect2
- */vrpn_client_node/RigidBody/pose*: raw poses from the motion capture system

The meaning of most topics is self-explanatory. All data use the time in the ROS system as the timestamp. The */flag_state* of NUC is a type *enum* and contains the flag signal of the LWIR camera with the following fields: *FlagOpen*, *FlagClose*, *FlagOpening*, *FlagClosing*, and *Error*. The last topic contains raw poses stored as both a vector and a quaternion from the motion capture system.

2) *Calibration Files*: Both the raw data and the calibration results are provided. The results include intrinsics of each camera and extrinsic parameters between cameras. Moreover,

the relative poses between the marker frame and the cameras are also included.

VII. EVALUATION METRICS

A. Accuracy

For evaluating the performance of motion estimation methods, two metrics are commonly used: absolute trajectory error (ATE) and relative pose error (RPE) [3]. ATE is the root mean squared difference between the ground-truth positions and the corresponding estimated positions with an optimal pose \mathbf{T} . This error is defined as

$$r_{ATE} = \min_{\mathbf{T} \in \text{SE}(3)} \sqrt{\frac{1}{n} \sum_{i=1}^n \|\mathbf{T}\mathbf{p}_i - \mathbf{p}_i^g\|}, \quad (1)$$

where \mathbf{p}_i^g denotes the i -th ground-truth position and \mathbf{p}_i denotes the corresponding estimated position. n is the number of associated poses by timestamps. ATE evaluates the global performance of the motion estimation. The RPE metric is defined as

$$r_{RPE} = \sqrt{\frac{1}{n_\Delta} \sum_{i=1}^{n_\Delta} \|\text{trans}(\mathbf{E}_i)\|}, \quad (2)$$

$$\mathbf{E}_i = \left(\mathbf{T}_i^{g-1} \mathbf{T}_{i+\Delta}^g \right)^{-1} \left(\mathbf{T}_i^{-1} \mathbf{T}_{i+\Delta} \right), \quad (3)$$

where \mathbf{T}_i^g denotes the ground-truth pose at time i . The result depends on the time interval Δ . RPE is more suitable for the evaluation of the performance of odometry, where local accuracy is critical for tasks.

B. Robustness

Under varying illumination conditions, robustness is crucial for visual motion estimation systems. Before evaluating the robustness, the degree of illumination variation should be estimated. The equation of the image formation model [26] in image coordinate $\mathbf{x} \in \mathbb{R}^2$ is defined as

$$I(\mathbf{x}) = G(tV(\mathbf{x})B(\mathbf{x})), \quad (4)$$

where t is the exposure time, $G(\cdot)$ is the camera response function, $B(\cdot)$ is the irradiance image, and $I(\cdot)$ is the observed pixel value. The pixel-wise attenuation factors are denoted by $V: \mathbb{R}^2 \mapsto [0, 1]$ (vignetting). In the dataset, since the FoV of the standard camera is limited, the imaging distortion is not significant. Besides, since the variation in illumination is severe and the exposure time is fixed, $I(\mathbf{x}) \approx \lambda B(\mathbf{x})$ where λ is a scalar factor. Based on this result, the degree of illumination variation between adjacent images can be defined as

$$\omega_i = \left\| \frac{S_i - S_{i+1}}{t_i - t_{i+1}} \right\|, \quad (5)$$

where S_i and t_i denote the standard deviation of the i -th image and the timestamp of i -th image, respectively. As shown Fig. 13, when the light is turned on and off, the calculated weight forms a peak on the graph to indicate that the scene lighting changes significantly.

With the metrics described above, the equations of weighted absolute trajectory error (WATE) and weighted

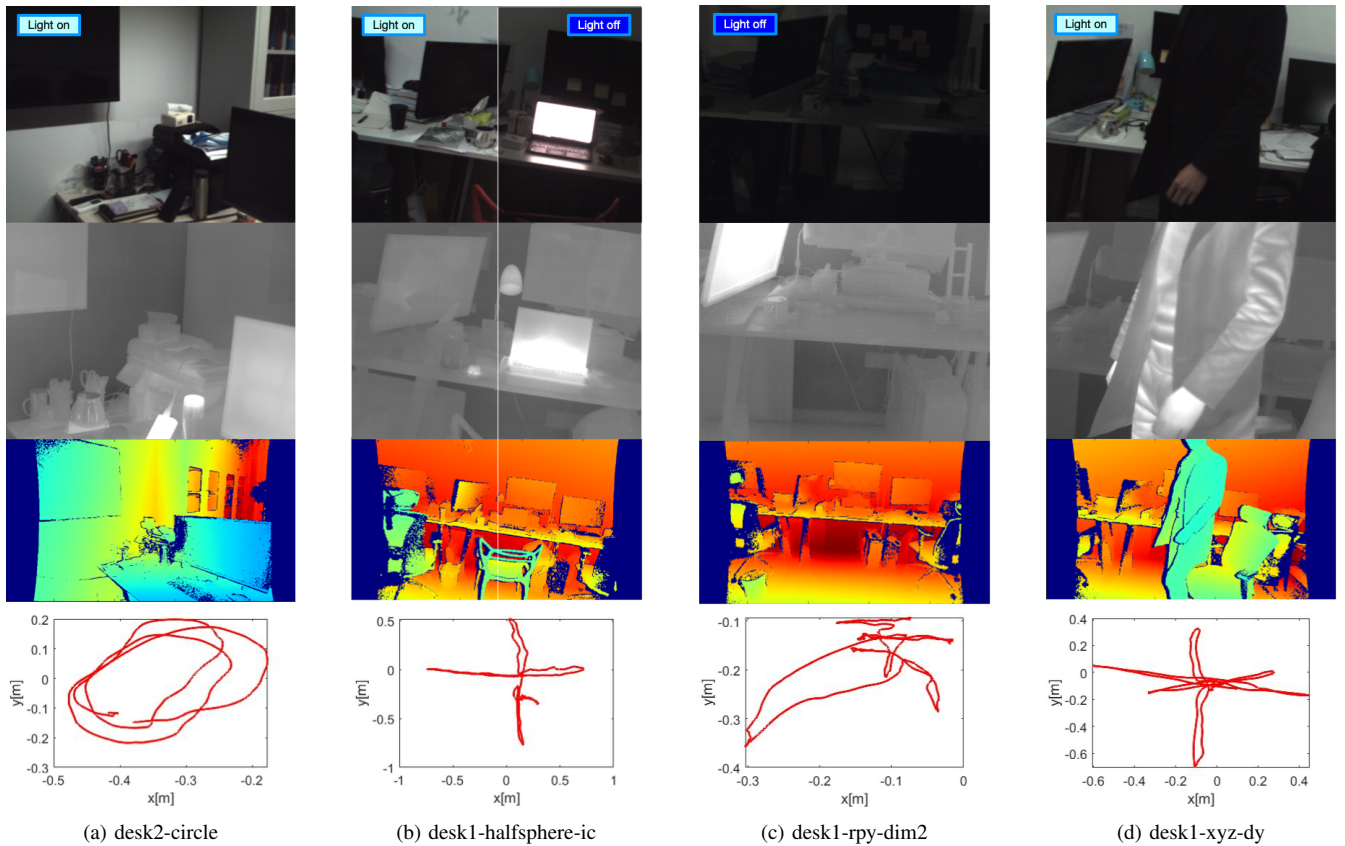


Fig. 11: Example of sequences. The images from top to bottom rows are color images, thermal images, depth images, and ground-truth trajectories. The color of depth images indicates the distance to the Kinect2.

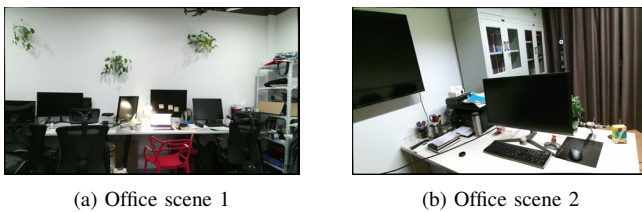


Fig. 12: Data acquisition environments. The curtains in both rooms are closed to avoid specular reflections since window glass is opaque across the LWIR spectrum.

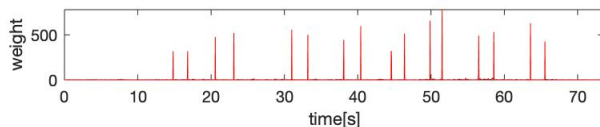


Fig. 13: The weights of desk1-halfsphere-ic. At the timestamps, when the lighting changes drastically, the calculated weight is significant. The images at the time of the first peak are shown in Fig. 11 (b).

relative pose error (WRPE) to evaluate robustness can be defined as

$$r_{WATE} = \min_{\mathbf{T} \in \text{SE}(3)} \sqrt{\frac{1}{\sum_{i=1}^n \omega_i} \sum_{i=1}^n \omega_i \|\mathbf{T}\mathbf{p}_i - \mathbf{p}_i^g\|}, \quad (6)$$

and

$$r_{WRPE} = \sqrt{\frac{1}{\sum_{i=1}^{n_\Delta} \omega_i} \sum_{i=1}^{n_\Delta} \omega_i \|\text{trans}(\mathbf{E}_i)\|}, \quad (7)$$

where each error is weighted. These two metrics make sense to increase the weight of the error when the illumination changes intensely.

VIII. CONCLUSIONS

In this paper, a novel dataset was proposed for evaluating the performance of multi-spectral motion estimation methods. The dataset includes sequences captured from different scenes with a diverse set of illumination conditions. In this dataset, the multi-spectral cameras were hardware-synchronized and well-calibrated. Highly accurate ground-truth poses were provided by a motion capture system for evaluation. Besides, depth images were provided for studying cross-modalities stereo matching. Some commonly used robustness metrics were also proposed. This dataset is publicly available with both raw and calibration data. It is hoped that this dataset can facilitate the development of all-day learning for multi-spectral motion estimation.

ACKNOWLEDGMENT

This work was supported by the National Natural Science Foundation of China (Grant No. 61673341), National Key R&D Program of China (2016YFD0200701-3), the Project

of State Key Laboratory of Industrial Control Technology, Zhejiang University, China (No. ICT1913), and the Open Research Project of the State Key Laboratory of Industrial Control Technology, Zhejiang University, China (No. ICT1900312).

REFERENCES

- [1] D. Scaramuzza and F. Fraundorfer, "Visual odometry [tutorial]," *IEEE robotics & automation magazine*, vol. 18, no. 4, pp. 80–92, 2011.
- [2] J. Fuentes-Pacheco, J. Ruiz-Ascencio, and J. M. Rendón-Mancha, "Visual simultaneous localization and mapping: a survey," *Artificial Intelligence Review*, vol. 43, no. 1, pp. 55–81, 2015.
- [3] J. Sturm, N. Engelhard, F. Endres, W. Burgard, and D. Cremers, "A benchmark for the evaluation of rgb-d slam systems," in *2012 IEEE/RSJ International Conference on Intelligent Robots and Systems*. IEEE, 2012, pp. 573–580.
- [4] A. Geiger, P. Lenz, C. Stillr, and R. Urtasun, "Vision meets robotics: The kitti dataset," *The International Journal of Robotics Research*, vol. 32, no. 11, pp. 1231–1237, 2013.
- [5] D. Schubert, T. Goll, N. Demmel, V. Usenko, J. Stückler, and D. Cremers, "The tum vi benchmark for evaluating visual-inertial odometry," in *2018 IEEE/RSJ International Conference on Intelligent Robots and Systems (IROS)*. IEEE, 2018, pp. 1680–1687.
- [6] P. Fankhauser, M. Bloesch, D. Rodriguez, R. Kaestner, M. Hutter, and R. Siegwart, "Kinect v2 for mobile robot navigation: Evaluation and modeling," in *2015 International Conference on Advanced Robotics (ICAR)*. IEEE, 2015, pp. 388–394.
- [7] J. Engel, V. Koltun, and D. Cremers, "Direct sparse odometry," *IEEE Transactions on Pattern Analysis and Machine Intelligence*, 2017.
- [8] C. Forster, Z. Zhang, M. Gassner, M. Werlberger, and D. Scaramuzza, "Svo: Semidirect visual odometry for monocular and multicamera systems," *IEEE Transactions on Robotics*, vol. 33, no. 2, pp. 249–265, 2017.
- [9] R. Mur-Artal and J. D. Tardós, "Orb-slam2: An open-source slam system for monocular, stereo, and rgb-d cameras," *IEEE Transactions on Robotics*, 2017.
- [10] A. R. Vidal, H. Rebecq, T. Horstschaefer, and D. Scaramuzza, "Ultimate slam? combining events, images, and imu for robust visual slam in hdr and high-speed scenarios," *IEEE Robotics and Automation Letters*, vol. 3, no. 2, pp. 994–1001, 2018.
- [11] F. Endres, J. Hess, J. Sturm, D. Cremers, and W. Burgard, "3-d mapping with an rgb-d camera," *IEEE transactions on robotics*, vol. 30, no. 1, pp. 177–187, 2013.
- [12] A. J. Davison, I. D. Reid, N. D. Molton, and O. Stasse, "Monoslam: Real-time single camera slam," *IEEE transactions on pattern analysis and machine intelligence*, vol. 29, no. 6, pp. 1052–1067, 2007.
- [13] H. Strasdat, J. M. Montiel, and A. J. Davison, "Visual slam: why filter?" *Image and Vision Computing*, vol. 30, no. 2, pp. 65–77, 2012.
- [14] K. Hajebi and J. S. Zelek, "Structure from infrared stereo images," in *Computer and Robot Vision, 2008. CRV'08. Canadian Conference on*. IEEE, 2008, pp. 105–112.
- [15] P. V. K. Borges and S. Vidas, "Practical infrared visual odometry," *IEEE Transactions on Intelligent Transportation Systems*, vol. 17, no. 8, pp. 2205–2213, 2016.
- [16] T. Mouats, N. Aouf, L. Chermak, and M. A. Richardson, "Thermal stereo odometry for uavs," *IEEE Sensors Journal*, vol. 15, no. 11, pp. 6335–6347, 2015.
- [17] A. Rankin, A. Huertas, L. Matthies, M. Bajracharya, C. Assad, S. Brennan, P. Bellutta, and G. W. Sherwin, "Unmanned ground vehicle perception using thermal infrared cameras," in *Unmanned Systems Technology XIII*, vol. 8045. International Society for Optics and Photonics, 2011, p. 804503.
- [18] T. Mouats, N. Aouf, A. D. Sappa, C. Aguilera, and R. Toledo, "Multispectral stereo odometry," *IEEE Transactions on Intelligent Transportation Systems*, vol. 16, no. 3, pp. 1210–1224, 2015.
- [19] W. Dai, Y. Zhang, D. Sun, N. Hovakimyan, and P. Li, "Multi-spectral visual odometry without explicit stereo matching," in *2019 International Conference on 3D Vision (3DV)*. IEEE, 2019, pp. 443–452.
- [20] D. Caruso, J. Engel, and D. Cremers, "Large-scale direct slam for omnidirectional cameras," in *International Conference on Intelligent Robots and Systems (IROS)*, 2015.
- [21] M. Burri, J. Nikolic, P. Gohl, T. Schneider, J. Rehder, S. Omari, M. W. Achtelik, and R. Siegwart, "The euroc micro aerial vehicle datasets," *The International Journal of Robotics Research*, vol. 35, no. 10, pp. 1157–1163, 2016.
- [22] M. Ferrera, V. Creuze, J. Moras, and P. Trouvé-Peloux, "Aqualoc: An underwater dataset for visual-inertial-pressure localization," *The International Journal of Robotics Research*, vol. 38, no. 14, pp. 1549–1559, 2019.
- [23] T. Pire, M. Mujica, J. Civera, and E. Kofman, "The rosario dataset: Multisensor data for localization and mapping in agricultural environments," *The International Journal of Robotics Research*, vol. 38, no. 6, pp. 633–641, 2019.
- [24] A. L. Majdik, C. Till, and D. Scaramuzza, "The zurich urban micro aerial vehicle dataset," *The International Journal of Robotics Research*, vol. 36, no. 3, pp. 269–273, 2017.
- [25] S. Leutenegger, S. Lynen, M. Bosse, R. Siegwart, and P. Furgale, "Keyframe-based visual-inertial odometry using nonlinear optimization," *The International Journal of Robotics Research*, vol. 34, no. 3, pp. 314–334, 2015.
- [26] J. Engel, V. Usenko, and D. Cremers, "A photometrically calibrated benchmark for monocular visual odometry," *arXiv preprint arXiv:1607.02555*, 2016.
- [27] S. Hwang, J. Park, N. Kim, Y. Choi, and I. So Kweon, "Multispectral pedestrian detection: Benchmark dataset and baseline," in *Proceedings of the IEEE conference on computer vision and pattern recognition*, 2015, pp. 1037–1045.
- [28] S. S. Shivakumar, N. Rodrigues, A. Zhou, I. D. Miller, V. Kumar, and C. J. Taylor, "Pst900: Rgb-thermal calibration, dataset and segmentation network," *arXiv preprint arXiv:1909.10980*, 2019.
- [29] C. Li, X. Liang, Y. Lu, N. Zhao, and J. Tang, "Rgb-t object tracking: benchmark and baseline," *Pattern Recognition*, vol. 96, p. 106977, 2019.
- [30] W. Treible, P. Saponaro, S. Sorensen, A. Kolagunda, M. O'Neal, B. Phelan, K. Sherbondy, and C. Kambhmettu, "Cats: A color and thermal stereo benchmark," in *Proceedings of the IEEE Conference on Computer Vision and Pattern Recognition*, 2017, pp. 2961–2969.
- [31] W. Maddern and S. Vidas, "Towards robust night and day place recognition using visible and thermal imaging," *RSS 2012: Beyond laser and vision: Alternative sensing techniques for robotic perception*, 2012.
- [32] Y. Choi, N. Kim, S. Hwang, K. Park, J. S. Yoon, K. An, and I. S. Kweon, "Kaist multi-spectral day/night data set for autonomous and assisted driving," *IEEE Transactions on Intelligent Transportation Systems*, vol. 19, no. 3, pp. 934–948, 2018.
- [33] E. Olson, "Apriltag: A robust and flexible multi-purpose fiducial system," *University of Michigan, Tech. Rep*, 2010.
- [34] Y. W. K. Zoetgnandé, A.-J. Fougères, G. Cormier, and J.-L. Dillenseger, "Robust low resolution thermal stereo camera calibration," in *Eleventh International Conference on Machine Vision (ICMV 2018)*, vol. 11041. International Society for Optics and Photonics, 2019, p. 110411D.
- [35] S. Vidas, R. Lakemond, S. Denman, C. Fookes, S. Sridharan, and T. Wark, "A mask-based approach for the geometric calibration of thermal-infrared cameras," *IEEE Transactions on Instrumentation and Measurement*, vol. 61, no. 6, pp. 1625–1635, 2012.
- [36] Z. Zhang, "A flexible new technique for camera calibration," *IEEE Transactions on pattern analysis and machine intelligence*, vol. 22, no. 11, pp. 1330–1334, 2000.